

Searching for helium escape and a low density atmosphere around the 120 Myr old sub-Neptune HIP94235b using CRIRES+

AVA MORRISSEY,¹ GEORGE ZHOU,¹ CHELSEA X. HUANG,¹ DUNCAN WRIGHT,¹ NEALE GIBSON,² KEIGHLEY E. ROCKCLIFFE,³
ELISABETH R. NEWTON,⁴ JAMES KIRK,⁵ AND DANIEL BAYLISS^{6,7}

¹University of Southern Queensland, Centre for Astrophysics, West Street, Toowoomba, QLD 4350, Australia

²School of Physics, Trinity College Dublin, University of Dublin, Dublin 2, Ireland

³Exoplanets and Stellar Astrophysics Laboratory, NASA Goddard Space Flight Center, Greenbelt, MD, USA

⁴Department of Physics and Astronomy, Dartmouth College, Hanover, NH 03755, USA

⁵Department of Physics, Imperial College London, Prince Consort Road, SW7 2AZ, London, UK

⁶Department of Physics, University of Warwick, Gibbet Hill Road, Coventry CV4 7AL, UK

⁷Centre for Exoplanets and Habitability, University of Warwick, Gibbet Hill Road, Coventry CV4 7AL, UK

Submitted to AJ

ABSTRACT

Atmospheric mass loss is thought to induce the bimodality in the small planet population as we observe it today. Observationally, active mass loss can be traced by excess absorption in spectral lines of lighter species, such as the hydrogen Ly- α line and the metastable helium triplet. We search for helium escape from the young (120Myr old) sub-Neptune ($3R_{\oplus}$) HIP94235b. We obtained two transit observations of HIP94235b using the Cryogenic InfraRed Echelle Spectrograph (CRIRES+) on the Very Large Telescope (VLT). We find no evidence for escaping helium across both visits, allowing us to place a mass loss rate upper limit of 10^{11}gs^{-1} , based on 1D Parker wind models. Additionally, we search for molecular spectral features in the planet's transmission spectrum, and cross-correlate our observations with high-resolution template spectra for H₂O, the dominating molecule in the Y-band. We detect no significant absorption. We demonstrate that some atmosphere models at $10\times$ solar metallicity would have been retrievable if present. Through the null detection of neutral hydrogen and helium escape, we conclude the atmosphere of HIP94235b likely lacks a large hydrogen-helium envelope. This is consistent with the expectation of small planet photoevaporation models, which suggest most planets lose their primordial hydrogen-helium envelopes within 100Myr of evolution.

Keywords: planetary systems — stars: individual (HIP 94235) techniques: spectroscopic, photometric

1. INTRODUCTION

Transit observations that span the metastable helium triplet of lines wavelength region allow for tracing of neutral helium escape from planets (Spake et al. 2018; Oklopčić & Hirata 2018). Although the first species used to trace atmospheric escape was the hydrogen Ly- α line (e.g. Vidal-Madjar & des Etangs 2003), the metastable helium triplet of lines offers a unique perspective with different advantages. The helium infrared triplet is

not affected by line core absorption from the interstellar medium (ISM). This expands the population of available planets suitable for observations beyond the ~ 50 pc limit imposed on equivalent Ly- α observations. The lack of ISM absorption also allows any planetary absorption to be measured over all velocity spaces, in contrast to being restricted to highly blue or red shifted outflows in the case of Ly- α . Helium, however, is most effective as a tracer of atmospheric escape around late type-stars (in particular K-type) due to their ionising potential, presenting limitations for observations of other stellar types (Seager & Sasselov 2000; Turner et al. 2016; Oklopčić 2019).

Detecting ongoing escape from young sub-Neptunes is one pathway to understanding the formation and evolution history of small close-in planets surrounding the radius gap. These small planets may have formed in gas-rich environments, and have low mean molecular weight gaseous envelopes surrounding rocky cores (e.g. Lee et al. 2014; Ginzburg et al. 2016). Alternatively, small planets may have formed in the water-rich parts of the protoplanet disk, and are composed of water-rich exteriors surrounding Earth-like cores (e.g. Zeng et al. 2019). Importantly, gaseous envelopes are most susceptible to undergo runaway mass loss, while heavier water-rich envelopes undergo less significant changes in the early lives of these planets (e.g. Lopez et al. 2012; Rogers et al. 2025).

Detections of helium escape have been reported for mature aged Neptune-sized planets previously, including HAT-P-11b (Allart et al. 2018; Mansfield et al. 2018; Guilluy et al. 2024) and GJ3470b (Palle et al. 2020; Niran et al. 2020; Guilluy et al. 2024). These planets orbit gigayear old systems, and are unlikely to undergo the runaway mass loss experienced by some Neptune-sized planets that would lead to large radial evolution over the 100 Myr timescale (Owen & Wu 2017; Ginzburg et al. 2018). Of the young planets surveyed so far, most have yielded non-detections of escaping neutral helium, including planets in the V1298 Tau (Alam et al. 2024; Orell-Miquel et al. 2024), TOI-1807 (Gaidos et al. 2023; Orell-Miquel et al. 2024), and K2-100 (Gaidos et al. 2020; Alam et al. 2024) systems. Tentative detections were reported for young (< 1 Gyr) sub-Neptunes in HD63433 c (~ 400 Myr) (Zhang et al. 2022), TOI-560b (480-750 Myr), TOI-1430.01 (165 ± 30 Myr), TOI-2076b (204 ± 50) and TOI-1683.01 (500 ± 150) (Zhang et al. 2023), though follow-up observations have failed to confirm some of these detections (Gaidos et al. 2023; Alam et al. 2024).

The presence of a low density gas-rich envelope should also be linked to the bulk density and atmospheric metallicity of the planets. JWST and HST observations of young sub-Neptune progenitors such as V1298 Tau b, V1298 Tau c (Barat et al. 2024b,a) and HIP67522b (Thao et al. 2024) (≤ 20 Myr) have Neptune-like masses and sub-solar metallicities. Older sub-Neptunes (> 1 Gyr), including GJ1214b (Gao et al. 2023), GJ9827d (Piaulet-Ghorayeb et al. 2024), TOI-836c (Wallack et al. 2024), GJ3090b (Parker et al. 2025) and GJ436b (Mukherjee et al. 2025), have been shown to have significantly enhanced atmospheric metallicities ($\geq 100x$ solar).

HIP 943235 b is a 120 ± 50 Myr old sub-Neptune orbiting a G-type host ($T_{\text{eff}} = 5991$ K, $1.094 M_{\odot}$, $1.08 R_{\odot}$)

on a 7.7 day period (Zhou et al. 2022). The continuum transit depth of HIP94235b is 600ppm, or 0.06%. Zhou et al. (2022) estimated the age of HIP94235 based on its association with the AB Doradus moving group. Additionally, the star’s stellar rotation rate, lithium abundance and x-ray emission intensity are all consistent with this age estimate. At 120 Myr old, HIP94235b offers a unique time frame to search for escape around a star whose intense XUV bombardment of its orbiting planets is exponentially declining. The relatively small size ($R = 3.00^{+0.32}_{-0.28} R_{\oplus}$) and age of HIP94235b present a rare opportunity to investigate the evolutionary transition of sub-Neptunes to super-Earths. The small size of HIP94235b in comparison to other young, pre-main sequence Neptunes (e.g. K2-33b, and those in the V1298 Tau system) may suggest it is more akin to the class of super-Earths around more mature stars, which makes it an important object for understanding the effects of atmospheric escape on the small planet population.

Morrissey et al. (2024) searched for traces of escaping neutral hydrogen from HIP94235b. Though a null detection was reported from two Lyman- α transit observations, significant interstellar extinction of the line over a distance of 58 pc prevented strong constraints from being placed on escape. In this paper, we present two transit observations of HIP94235b with the infrared high resolution spectrograph CRRES+ (the recently upgraded CRyogenic high-resolution InfraRed Echelle Spectrograph) to search for traces of helium escape from the sub-Neptune. These helium observations are unobstructed by interstellar absorption, and any escaping tails are affected by the stellar ionizing irradiation differently to that from neutral hydrogen, and as such provide a new dimension to constraining the atmospheric composition and evolution of this sub-Neptune system. We also search for transmission spectroscopic signatures from water vapour in the atmosphere of the planet. Detections of such signatures are expected if the planet hosts a low metallicity, low mean molecular weight atmosphere that may still remain post formation.

2. OBSERVATIONS AND SPECTRAL EXTRACTION

2.1. Observations

We obtained two visits of HIP94235b with CRRES+ on the VLT in La Paranal, Chil e (Dorn et al. 2023). For both of our visits on July 14th and August 15th 2023, CRRES+ observed HIP94235b for one half of each night, spanning 5.5 hours total observing time each visit. Observations in Visit 1 began two hours pre-ingress, and continued to observe the target through to 45 minutes post-egress. Observations in Visit 2 began

Target	HIP94235b
Programme ID	111.24TH.001(2023-07-15), 111.24TH.002(2023-08-15)
Instrument	CRIRES+
Filter	Y1029
Wavelength Coverage	950-1120 nm
Exp. Time	1x900s
AO	No (.001), Yes (.002)
Airmass	See Fig. 1
Seeing	See Fig. 1
Slit	0.2"

Table 1. Overview of both visits of HIP94235b using CRIRES+. Visit 1 is denoted as .001 and Visit 2 is denoted as .002. The exposure time of 1x900s represents NDITxDIT, which is the number of detector integrations x detector integration time.

3 hours and 20 minutes pre-ingress, obtaining a solid pre-transit baseline. For both visits, CRIRES+ was operating at maximum resolution of $R = 92000$ through the use of the 0.2" slit. HIP94235 has a brightness of $V = 8.31 \pm 0.03$ in the optical (Henden et al. 2016) and $K = 6.881 \pm 0.027$ in the infrared (Skrutskie et al. 2006). The slit is placed at 90° with respect to sky to minimize the effects of atmospheric dispersion over the slit. A nodding pattern of ABBA was adopted for both visits to allow for efficient background removal. Visit 1 is broken up into 62 observations: 31 from nodding position A and 31 from B. Within each observation, there are nine spectral orders, corresponding to different wavelength regions across the spectrograph. Similarly, 28 observations in each nodding position were obtained in visit 2. Visit 2 observations benefited from adaptive optics corrections, with the target star acting as the natural guide star. Wavelength calibration is provided via day-time Neon/Krypton lamp exposures, as is standard to support CRIRES observations. Table 1 outlines a summary of the observations, and environmental variations over the course of the two nights are presented in Figure 1.

2.2. Spectral Extraction and calibration

We made use of PYCRIRES, a data reduction pipeline for VLT/CRIRES+ (Stolker & Landman 2023), a python wrapper for CRIRES+ pipelines of ESOREX, for calibration and spectral extraction. Figure 2 shows one example extracted spectrum for Visit 1. Each order in the upper panel shows the raw spectra prior to normalization and telluric correction. The edges of each order have been trimmed by 50 pixels on each side.

The lower panel depicts order 2, spanning the 1077 - 1084nm wavelength range, surrounding the 1083 nm metastable helium triplet of lines. The spectrum in the lower panel has been corrected for telluric absorption, following processes described in Section 2.3.

2.3. Telluric correction

We make use of the TELFIT script for telluric correction of our observed spectra (Clough et al. 1992; Gullikson et al. 2014). Telfit models the temperature, pressure, telescope zenith angle, and abundances of the telluric atmosphere, and wavelength offsets of the input dataset. This is performed iteratively while also accounting for the stellar spectrum via the PHOENIX model library (Hauschildt et al. 1999).

Examples of the telluric corrected spectra are shown in Figure 2. Strong and saturated telluric lines remain poorly subtracted after this procedure, and are masked out manually for further analysis. Orders 1, 8 and 9 are heavily contaminated by tellurics, so we discarded these orders for further analysis.

3. SEARCHING FOR NEUTRAL HELIUM ESCAPE

3.1. Removal of stellar signal

Post-telluric calibration, we corrected for stellar contamination via a median division of an observed master template. We computed the median stellar spectrum from out-of-transit exposures and divided it from each individual exposure, removing quasi-static stellar features while preserving time-dependent signals. We applied this method to all orders for each observation across both nights, producing residual maps for further analysis. Fig 3 shows the effect of this approach on visit 1 of the CRIRES+ data. The upper panel shows the observed spectra before median removal, while the lower panel presents the residuals after the stellar removal. A discussion of SYSREM and why it is not suitable to this dataset and this planet is provided in Section 4.4.

3.2. Search for excess helium absorption

Fig 4 shows the spectral residuals over the helium infrared triplet as seen over both visits. Over-plotted are lines marking the expected radial velocity variation of the planet, and the times of ingress and egress. We detect no significant excess absorption or variability of the helium triplet from these spectral residuals.

Before computing the helium absorption light curve, we first shifted each spectrum to the planetary rest frame using it's radial velocity before combining them. Then, to quantify any flux variability over the helium lines, we compute the total flux over the helium infrared triplet over each exposure. We integrated within 0.15nm

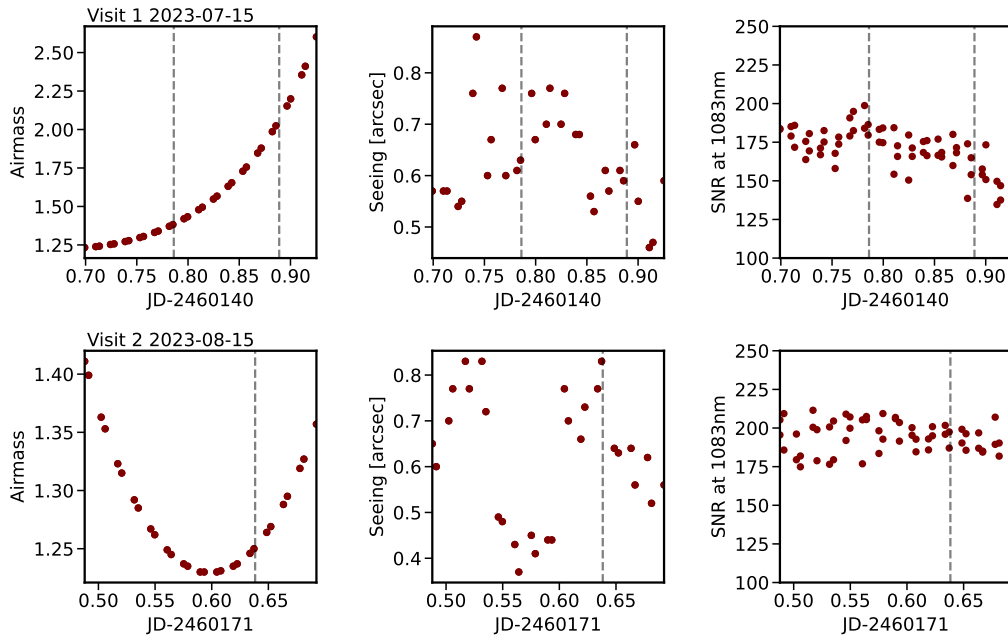


Figure 1. Environmental variations over the course of both transit observations. Included are variations in airmass, seeing, and per pixel signal to noise over the helium triplet at 1083 nm over the course both nights. The vertical lines across all plots represent times of ingress and egress for both visits, respectively.

of the main helium triplet peak at 1083.33 nm, as per Zhang et al. (2023) to calculate the helium lightcurves, shown in Fig 5 for both visits. We detect no variability over the helium wavelength over the course of the planetary transits.

To determine mass loss upper limits that can be established, we first fit for the shallowest transit depth that would be detectable in these observations. We model the transit as per Mandel & Agol (2002) via the BATMAN code Kreidberg (2015). We allow R_p/R_* to be a free parameter, while holding the remaining transit parameters constant, including a/R_* , inclination, and transit period and centroids as per the white light transit. We find we can place a 5σ upper limit of $R_p/R_* < 0.03919$ (< 0.0015 in transit depth) via the posterior distribution.

To convert this transit depth limit to a mass loss limit (\dot{M}), we make use of the P-WINDS Parker-winds model (Dos Santos et al. 2022). P-WINDS is a 1-D wind model designed to simulate the interaction between the XUV flux of a host star and the escaping hydrogen and helium from the orbiting planet. The model depends on key system parameters, including stellar flux, planetary composition, and atmospheric structure, to predict mass loss rates. We make a number of assumptions in this model, the temperature of the upper planetary atmosphere is set to 6000 K, with the hydrogen number fraction assumed to be 0.9, and the remaining 10% allocated to helium. Adopting the same approach as Morrissey et al.

(2024), we scaled the XUV flux from the 100 Myr old G-type star EK Dra (Ribas et al. 2005) to estimate the incident flux for HIP94235b.

Example transit models with depths corresponding to reasonable mass loss rates are over-plotted in Figure 5. From these, we place a 5σ upper limit constraint on the ongoing mass loss rate of HIP94235b as 10^{11}gs^{-1} , or $0.53 M_\oplus/\text{Gyr}$. Specifically, we find mass-loss rate constraints of $7.5 \times 10^{10} \text{gs}^{-1}$ for visit 1, $3.9 \times 10^{10} \text{gs}^{-1}$ for visit 2 and $3.9 \times 10^{10} \text{gs}^{-1}$ from a joint fit to both visits. We report our final upper limit as 10^{11}gs^{-1} , rounded up to one significant figure to reflect the uncertainties associated with our use of a simplified one-dimensional Parker wind model through our use of *p-winds*, and to emphasize that our results are constrained on the order of magnitude level.

3.3. Constraining planet mass loss evolution history

We follow Morrissey et al. (2024) and constrain XUV driven photoevaporation tracks via the mass loss upper limits we determined from the helium null detection. We model the radius and envelope mass evolution of HIP94235b as per the energy limited approximation detailed in Owen & Wu (2017), finding sets of models that will fit the current age and radius of the planet. We free the core mass, initial envelope fraction, and mass loss efficiency η of the planet.

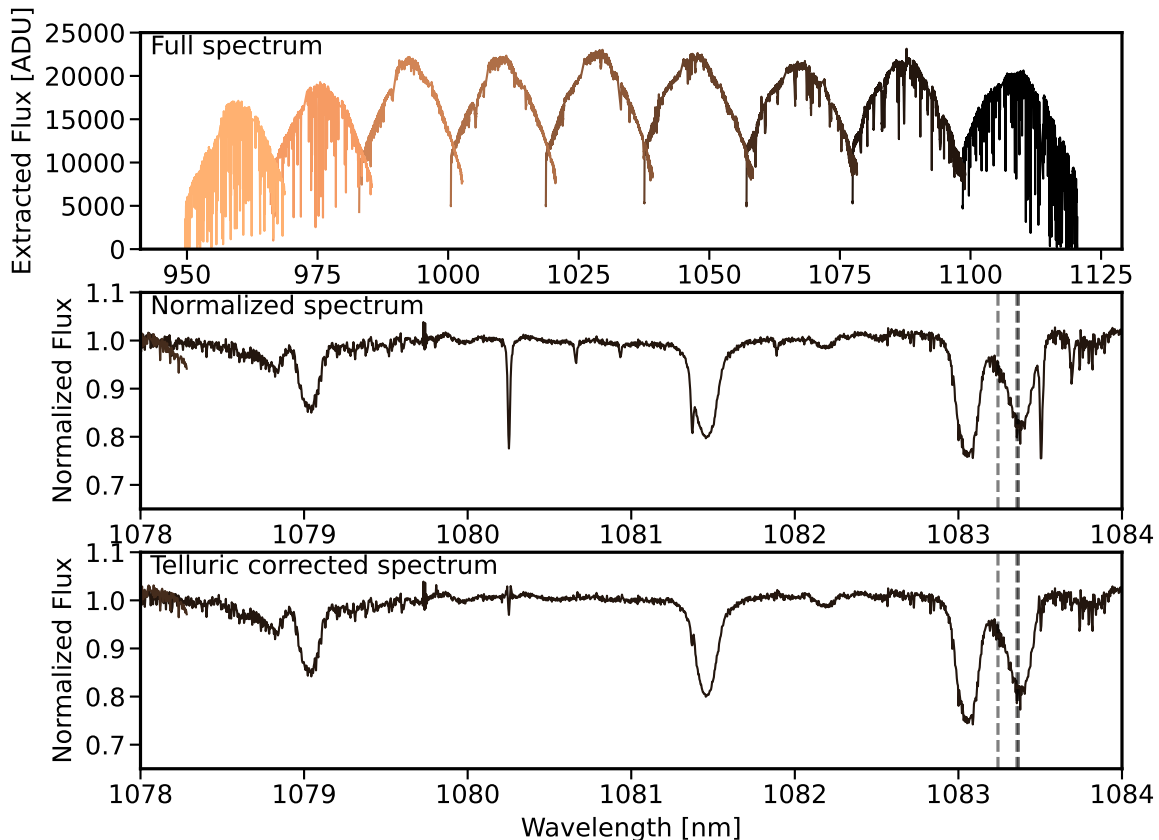


Figure 2. One example CRRES+ spectrum of HIP94235b obtained during visit 1. **Top** Extracted spectrum from all nine spectral orders, arranged in descending order from left to right, with order 9 on the far left and order 1 on the far right. **Middle** Normalized stellar spectrum over the helium infrared triplet at 1083 nm. The wavelengths of the helium infrared triplet are marked by the vertical lines. **Bottom** Telluric corrected portion of the spectrum over the helium infrared triplet region.

Figure 6 shows the allowed set of models that can replicate the present day radius of HIP94235b. Without the helium mass loss constraints, the current conditions can be reproduced with a wide range of initial envelope mass fractions, ranging from 3% to 100% gas in composition, with corresponding core masses ranging from 2 to $10 M_{\oplus}$.

Incorporating the observationally determined mass loss rate constraint of $\dot{M} < 10^{11} \text{gs}^{-1}$, these evolution models can be significantly constrained. In particular, the initial envelope mass fraction is expected to be 3–10% of the mass of the planet.

From these energy limited models, we find the low mass loss rate of HIP94235b is still consistent with having been born in a gas rich environment. Rogers & Owen (2021) showed the *Kepler* small planets can be replicated by a population of ‘gas dwarfs’ with initial gas envelopes that follow a β distribution with a mean of $\sim 4\%$ in total planet mass. Significantly gas rich scenarios are likely ruled out for HIP94235b. Recent HST and JWST

observations of the planets around the young systems of V1298 Tau (Barat et al. 2024b,a) and HIP67522b (Thao et al. 2024) showed they may consist with gas envelopes $\sim 40\%$ in mass fraction. Such low density young planets are unlikely to be progenitors of HIP94235b.

4. HIGH RESOLUTION SEARCH FOR TRANSMISSION SPECTROSCOPIC FEATURES

We also make use of the Y-band transit observations to search for additional spectral features in the atmosphere of HIP94235b. We cross correlate the CRRES+ spectral residuals against planetary spectral templates to search for signatures of water vapor in the atmosphere of the planet.

4.1. Synthetic model spectra

To generate model spectra for cross-correlation with our observations, we used the radiative transfer code PETITRADTRANS (Mollière et al. 2019). PETITRADTRANS computes high resolution synthetic planetary

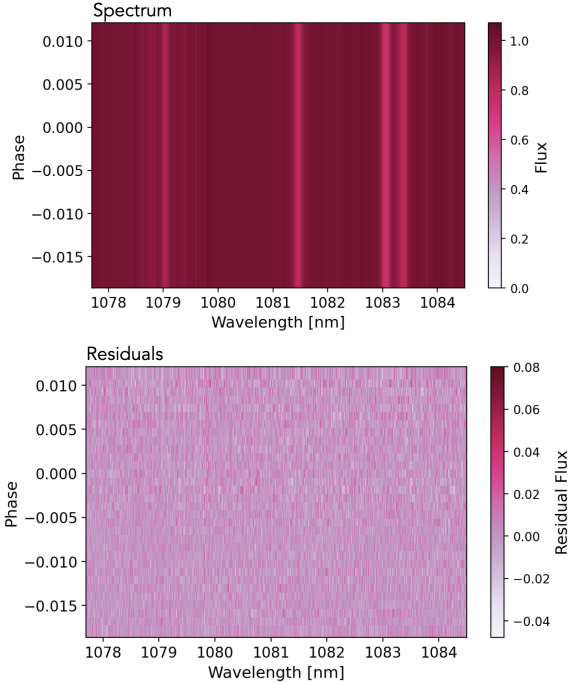


Figure 3. We make use of a median out-of-transit stellar spectrum to remove the stellar spectral signal over the helium line triplets range. Temporal variations of the stellar spectrum are shown. The median removal is performed on a per-visit, per nodding position basis, as each visit and nodding position has its own associated systematics. **Top:** Observations over the first CRIRES+ visit, from nodding position A, prior to median division. Stellar absorption features appear as deep vertical stripes that are constant in velocity within the stellar rest frame. **Bottom:** The spectral residuals after applying median division, demonstrating the removal of stellar spectral features while preserving any potential planetary signal.

transmission spectra via a line-by-line radiative transfer model.

We include absorption from water vapor, methane, carbon dioxide, and carbon monoxide in our line by line model. We also incorporated the effects of Rayleigh scattering via H_2 and He, alongside collision-induced absorption (CIA) from H_2 - H_2 and H_2 -He interactions.

The model atmospheres were computed over a pressure range of 10^{-10} - 10^2 bar using 130 logarithmically spaced points. The temperature-pressure (T-P) profile was computed using the analytical radiative equilibrium model from Guillot (2010). Our chosen inputs for the infrared opacity (κ_{IR}), the ratio of optical to infrared opacity (γ), intrinsic temperature and equilibrium temperature were 0.01, 0.4, 200K and 1060K, respectively. Mixing ratios are computed via the grid from EASY-CHEM (Mollière et al. 2017), interpolated via the INTERPOL ABUNDANCES function in PETITRADTRANS.

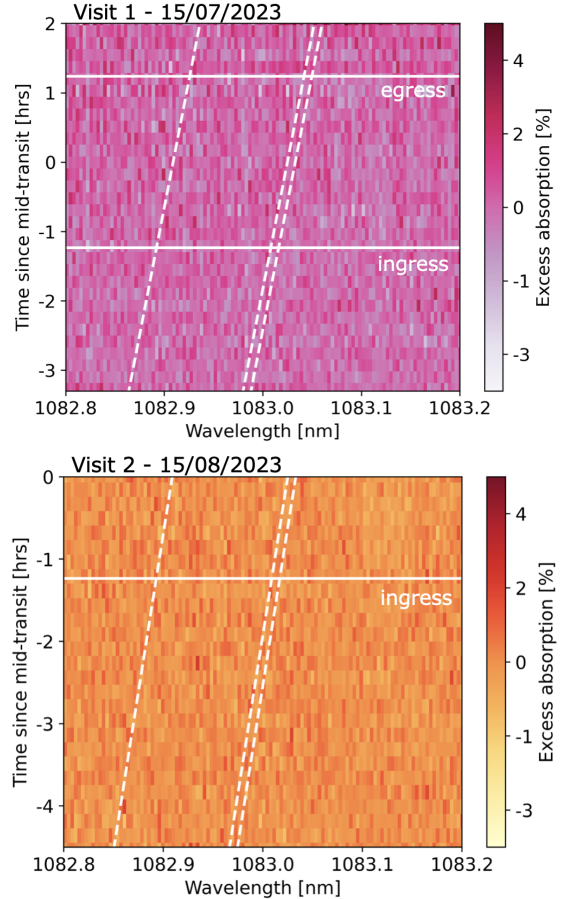


Figure 4. Spectral residuals as a function of time since mid-transit (hours) and wavelength (nm). Visit 1 is in pink and visit 2 is in orange. The solid horizontal lines represent ingress and egress. The slanted dashed lines mark the wavelengths of the metastable helium triplet of lines, Doppler shifted to the rest frame of the planet. The colorbar on the right represents the amount of excess absorption within the plot in percent.

We adopt system parameters for HIP94235b from Zhou et al. (2022). We assume a planet mass of $5 M_{\oplus}$ for a low density sub-Neptune model with 2% H_2 envelope at $3 R_{\oplus}$ (Zeng et al. 2019). We assume a cloudless atmosphere of solar metallicity, with a mean molecular weight of 2.3 atomic mass units, for our cross correlation analyses. The synthetic spectrum is shown in Figure 7.

The model transmission spectra were computed using the CALC TRANSM function from PETITRADTRANS, which solves the radiative transfer equation throughout a limb geometry to determine the effective transit radius as a function of wavelength. We defined the planetary radius and gravity at a pressure level of $P_0 = 0.01$ bar, providing the baseline for computing variations in spectral opacity along the planet’s limb.

Given the resolving power of CRIRES+ ($R = 100,000$),

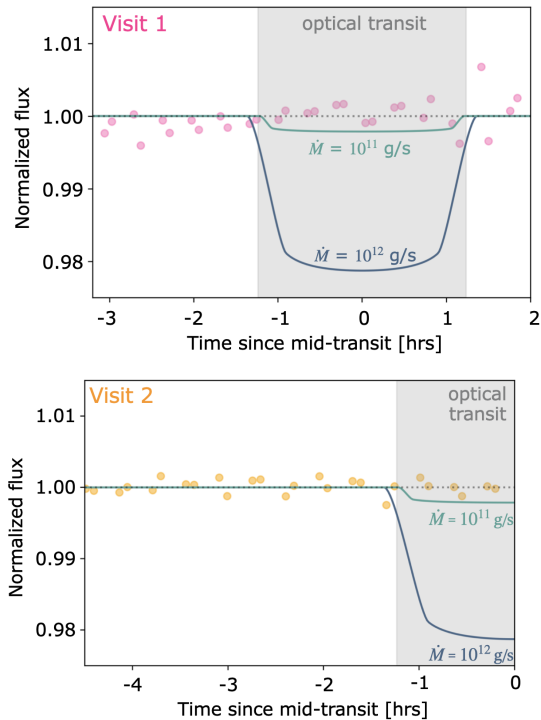


Figure 5. Lightcurves for visit 1 (top) and visit 2 (bottom) that trace along where we would expect the metastable helium triplet of lines to be present. The optical transit of HIP94235b is depicted by shaded grey regions. Lightcurves with transit depths based on different mass loss rates are shown in teal ($\dot{M}=10^{11}\text{gs}^{-1}$) and blue ($\dot{M}=10^{12}\text{gs}^{-1}$).

spectral features can be resolved down to a velocity difference of $\text{FWHM}\sim 3\text{ km/s}$. To account for this instrument broadening, we defined a Gaussian function with a velocity dispersion of 3 km/s to match the resolving power. We then convolve the model spectrum with this Gaussian kernel to simulate the effects of instrumental broadening on our PETITRADTRANS model spectra.

4.2. Stellar and telluric spectral removal

Preparation of the observed spectra for cross correlations is performed similar to the procedure described in Section 3. A telluric model was fitted for and removed from each observation via the TELFIT code as per Section 2.3. An example of one resulting stellar spectrum is shown in Figure 7. As per the helium excess analysis, we extracted spectral residuals via the removal of a median spectrum. A master median combined spectrum was generated for each nodding position on each night using only the out of transit spectra, and removed from corresponding individual observations. This median master spectrum was generated at the stellar rest frame first. A second iteration of removals is performed

at the telluric rest frame to remove any additional signals. The use of median spectral division over SYSREM is motivated by the slow velocity variation of the planet over the course of the transit ($< 10\text{ km s}^{-1}$). In section 4.4, we demonstrate that it is difficult to preserve the planetary signal and efficiently remove stellar and telluric signals via SYSREM.

Spectral regions near the detector edge, and regions heavily influenced by telluric absorption were manually masked from the dataset. Additionally, orders 1, 6, 8 and 9 were excluded from further analysis due to excessive noise (see Figure 7 for masked spectra).

4.3. Cross-Correlation analysis

The spectral residuals from each epoch are cross correlated against our high resolution synthetic spectral template. A cosine apodization function was applied to the observed spectra to minimize edge effects. Cross correlation functions (CCFs) were computed over a velocity range of -300 to $+300\text{ km s}^{-1}$ using a Doppler step of 3 km s^{-1} .

Cross correlation functions from select orders that are not telluric dominated (see Figure 7) are median combined into one master cross correlation function per epoch. To remove common systematics that may still be present for all epochs, we also remove the common cross correlation function median combined over all epochs. This median correlation function is constructed for each night and each nodding position separately.

The temporal variations in the cross correlation function are presented in Figure 8. The expected radial velocity variation of HIP94235b over the course of the observations are marked, along with the expected times of ingress and egress. We find no significant planetary absorption over the Y-band from the two CRIRES+ transit observations.

If a planetary signal is present, we would expect the detection of excess absorption at the correct orbital and systemic velocity of HIP94235b. We map the signal to noise of our observations over a grid of orbital K_p and systemic V_{sys} velocities. For each K_p and V_{sys} grid point, we velocity shift and interpolate the cross correlation functions from each epoch to the rest frame of the planet, and median combine all in-transit observations over the two transits. To estimate the signal at each grid point, we follow previous examples (e.g. Brogi et al. 2018; Gibson et al. 2020) and measure the cross correlation function peak height over a central $\pm 2\text{ km s}^{-1}$ region. The noise in the combined cross correlation functions is characterized by the standard deviation in this peak height over velocity spaces surveyed

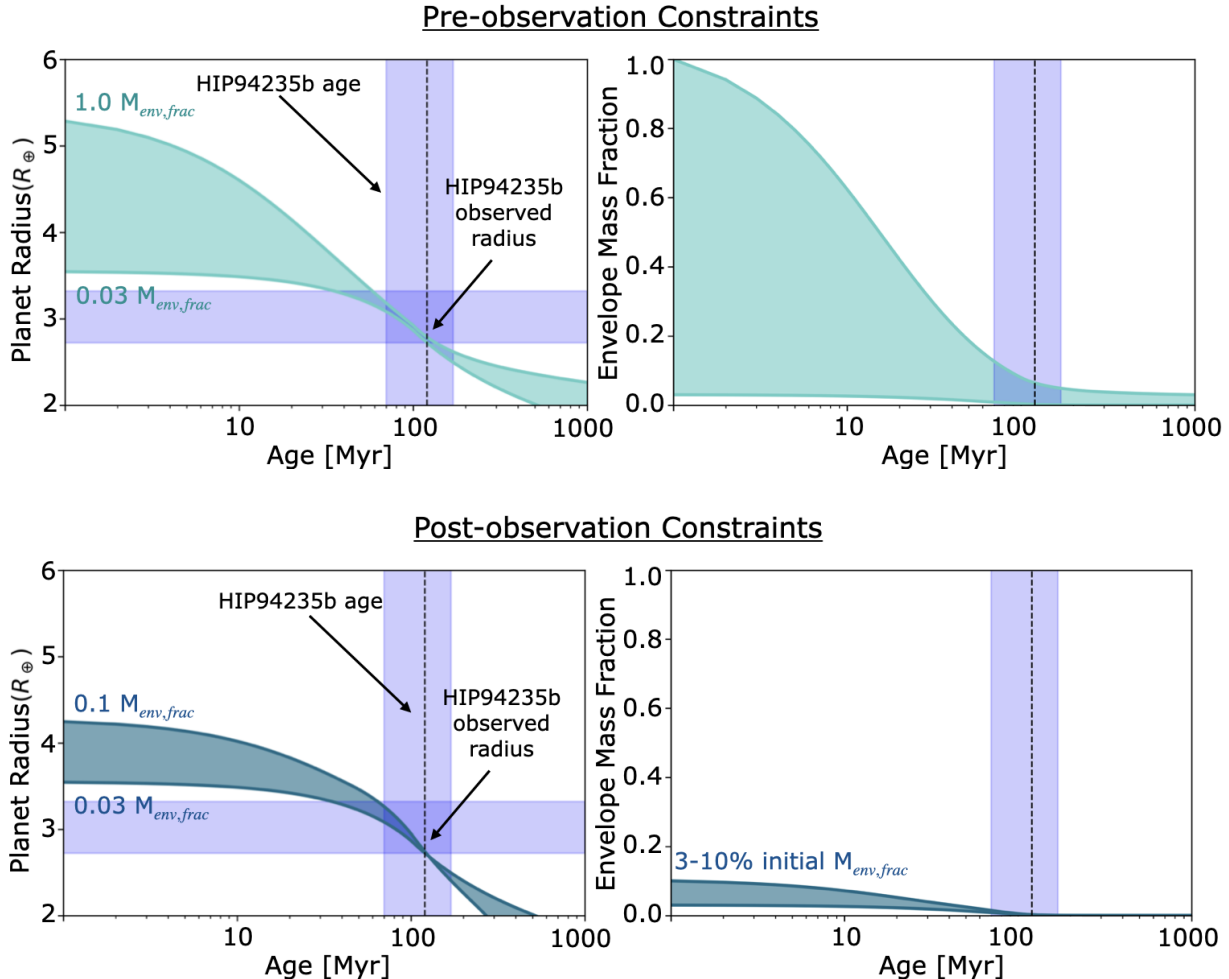


Figure 6. Evolution tracks for HIP94235b’s radius (left) and envelope mass fraction (right) evolution over the first Gyr. The top panel shows the allowed tracks before these CRIFRES+ results, with the bottom panel showing the observationally constrained tracks. HIP94235b has formed with a radius of 3.5–4.2 R_{\oplus} and an initial envelope mass fraction of 3–10%. The transparent blue bars in each figure show the error on the planet radius ($R = 3.00^{+0.32}_{-0.28} R_{\oplus}$) as the horizontal transparent region, and planet age (120 ± 50 Myr) as the vertical transparent region.

at $|K_p| > 200 \text{ km s}^{-1}$ and systemic $|V_{\text{sys}}| > 200 \text{ km s}^{-1}$. Figure 9 shows the signal to noise map over a range of reasonable orbital and systemic velocities. No significant absorption is identified at the velocities of the planetary system of $K_p = 111 \text{ km s}^{-1}$ and $V_{\text{sys}} = 9 \text{ km s}^{-1}$ (Zhou et al. 2022; Gaia Collaboration et al. 2021). We note the eccentricity of the planet is not well constrained from photometry alone, and as such a detection at different V_{sys} and K_p velocities would still have been acceptable as a planetary signal, with the effect of eccentricity on a detection shown in Figure 4 of Grasser et al. (2024) for GJ 436b.

4.4. Injection and recovery tests

To quantify the detectability of planetary signals in our observations and our analyses, we inject the synthetic planetary template into our observations and test

for its recoverability. We adopt the synthetic template generated in Section 4.1, and inject it into the extracted observed spectra prior to telluric and stellar removal. The injection is performed at the predicted orbital radial velocity of the planet and at a systemic velocity of -25 km s^{-1} to avoid overlapping with any potential intrinsic planetary signal.

The spectra are then cross correlated as per section 4.3, and the signal detection is evaluated via the K_p - v_{sys} grid. We find that a $5 M_{\oplus}$ solar metallicity cloudless planet model can be recovered when the datasets from both nights are combined at the 2σ level (Figure 10). We also found $10\times$ solar metallicity template, at $5 M_{\oplus}$, can be retrieved at the 3.0σ level. We note that though a template of solar abundance was adopted, the only effective absorber in the Y-band is H_2O . Injection and

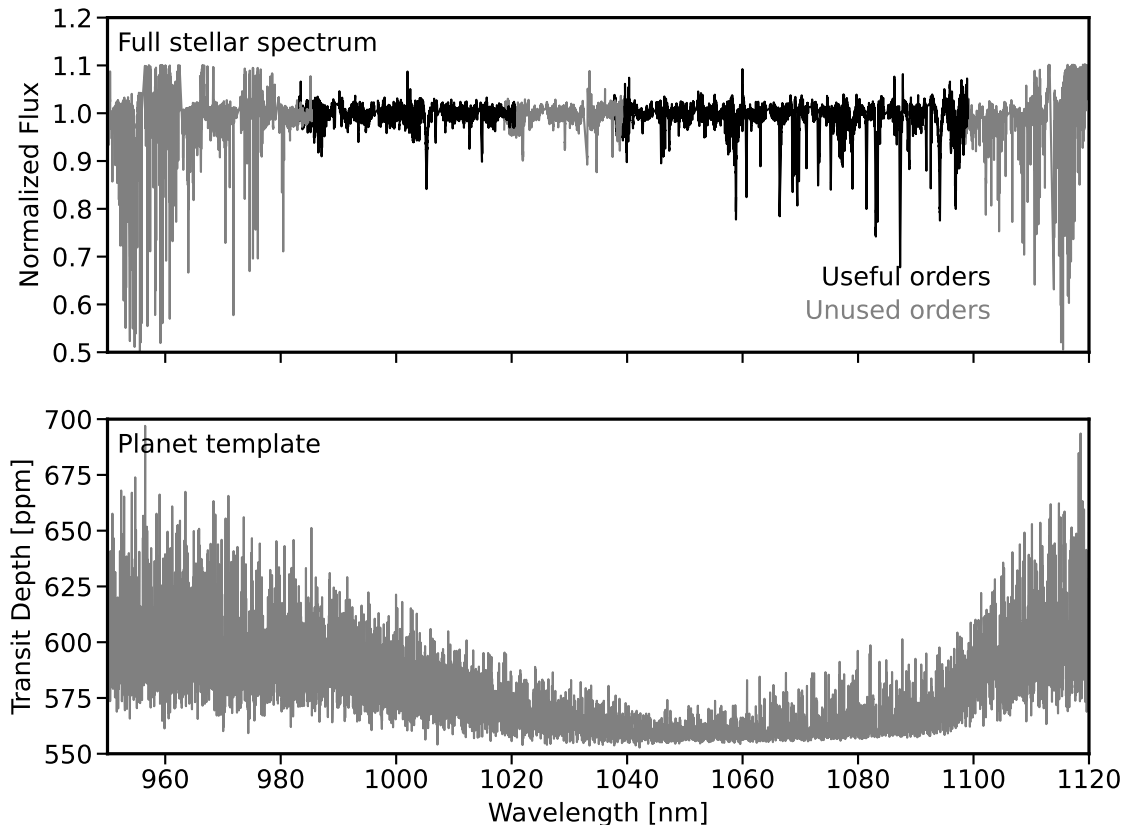


Figure 7. **Top** The normalized and telluric corrected stellar spectrum over all orders are plotted, arranged in descending order from left to right, with order 9 on the far left and order 1 on the far right. Orders with observations included in our cross correlation analyses are marked in black, orders discarded in gray. **Bottom** The input synthetic transmission spectrum for a $3 R_{\oplus}$, $5 M_{\oplus}$ planet hosting a clear, solar metallicity atmosphere is plotted. All modeled lines within the spectral region observed come from water absorption.

recovery of other absorbers, including CO, CO₂, and CH₄, show the observations are not capable of providing meaningful constraints on their presence, unsurprising given the lack of significant absorption features in the observed wavelengths of our observations.

We also performed the same analysis, but making use of the SYSREM algorithm (Tamuz et al. 2005) to remove the stellar spectrum instead of median division. We found the injected planetary signal cannot be recovered if SYSREM is adopted (see bottom plot of Figure 10). We attribute this to the low velocity variation of the planet during the transit, resulting in the removal of the planetary signal alongside the stellar signal via SYSREM.

We also performed a series of injection and recoveries for a range of other atmosphere models, ranging between M_p of 5 - $10 M_{\oplus}$ and metallicities of 1 - $500\times$ solar. We find the only model that can be retrieved at the 3σ level is the $10\times$ solar metallicity $5 M_{\oplus}$ template. Since no

Table 2. Retrieval significance for injection and recovery of transmission signal

	$5 M_{\oplus}$	$10 M_{\oplus}$
$1\times$ Solar	2.1σ	1.4σ
$10\times$ Solar	3.0σ	2.1σ
$100\times$ Solar	2.4σ	2.0σ
$500\times$ Solar	1.8σ	1.5σ

mass constraint is available for this planet due to the activity and rapid rotation of the target star, we can only conclude that a solar metallicity atmosphere is unlikely if the planet is of low density. The recovery significance from these simulations are presented in Table 2.

5. DISCUSSIONS AND CONCLUSIONS

We obtained Y-band observations of the 120 Myr system HIP94235 via CRIRES+ on the VLT during the transits of its 7.7 day period sub-Neptune. These ob-

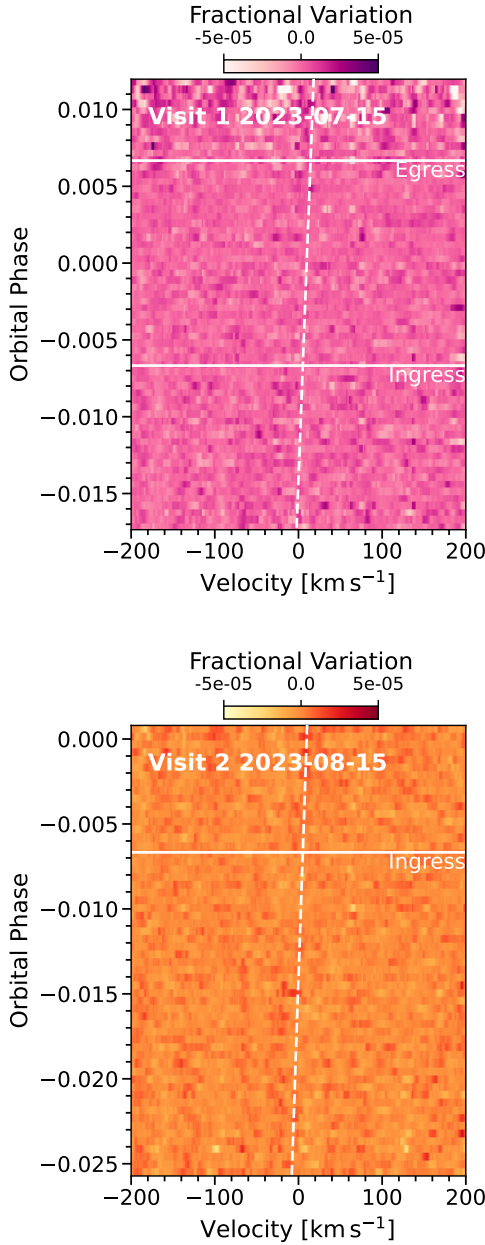


Figure 8. Cross correlation function variations over the two transit visits. Cross correlations are performed against a high resolution line by line spectral model of a $3 R_{\oplus}$, $5 M_{\oplus}$, solar metallicity atmosphere. The expected velocity variation of the planet, assuming a circular orbit, over the observations is marked by the dashed line. The times of ingress and egress are marked by the horizontal lines.

servations were used to search for signatures of excess helium absorption that may be attributable to mass loss from the young planet. We also searched for additional absorption from the presence of water in the atmosphere of this sub-Neptune.

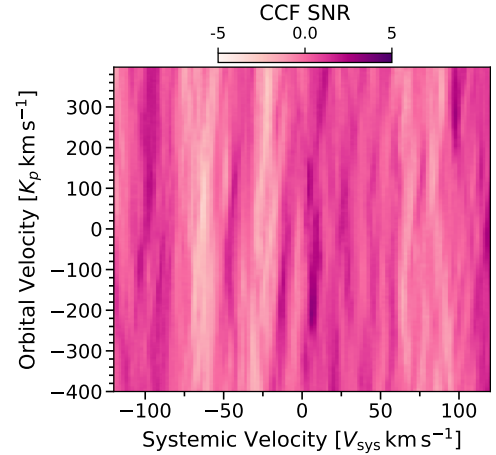


Figure 9. Cross correlation peak signal to noise as a function of the assumed orbital and systemic velocities of the planet, averaged over both nights of observations. For a circular orbit, the expected velocities of the planetary system are $K_p = 111 \text{ km s}^{-1}$ and $V_{\text{sys}} = 9 \text{ km s}^{-1}$. We find no evidence of excess absorption originating from the planet.

No excess helium absorption was detected for HIP94235b. The lack of mass loss detection is consistent with constraints placed via Lyman- α null detections of the same planet from Morrissey et al. (2024). Adopting 1D Parker wind models from Dos Santos et al. (2022), we place a mass loss rate upper limit of 10^{11} g s^{-1} for the planet. This mass loss rate limit is consistent with photoevaporation models that limit the initial envelope mass fraction to $< 10\%$ of the total mass of the planet. Larger initial envelopes would have yielded stronger active mass loss rates at the current age of the planet. Rogers & Owen (2021) found similar gas envelope fractions can reproduce the close in super-Earth and sub-Neptune planet population from *Kepler*.

In contrast, larger low density young planets, such as HIP67522 b (Thao et al. 2024) and V1298 Tau b and c (Barat et al. 2024b,a), have transmission spectra consistent with low density low metallicity atmospheres. The gas rich envelopes for these planets are expected to account for $\sim 40\%$ of the mass of the planet. If HIP 94235 b had progenitors similar to HIP67522 b and V1298 Tau b, we would have detected mass loss in our helium observations.

We also searched for atmospheric water absorption in the transmission spectrum of HIP94235b. We report no detectable signatures from two transit visits. We show via injection and recovery exercises that select models of cloudless atmospheres are retrievable if present.

Ground based high resolution transmission spectroscopy has been attempted for few Neptune-sized planets. Basilicata et al. (2024) report detections of

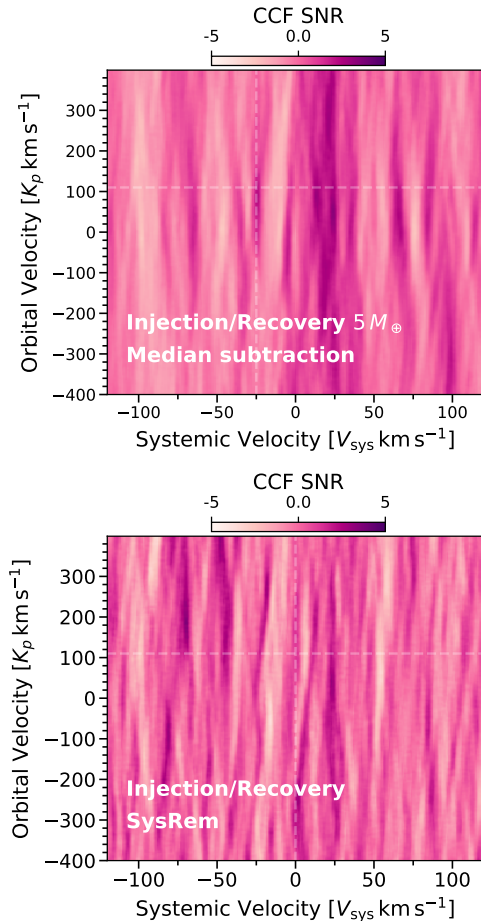


Figure 10. Recovery of the injected transmission signal of a clear, solar metallicity planetary model. **Top** We find the planetary signal can only be recovered at the 2σ level when the stellar signals are subtracted via a simple removal of the median spectrum. **Bottom** SYSREM removal of the stellar signal (over 4 iterations) removes the injected planetary signal, with no signals retrieved. The velocities of the injected signal are marked by the dashed lines.

H_2O and NH_3 in the atmosphere of HAT-P-11b via GIANO-B observations spanning the wavelength range of 950 – 2450 nm on the Telescopio Nazionale Galileo. The atmosphere of GJ 436 b was probed by CRIRES+ over the wavelength range of 1490-1780 nm, with a null detection of atmospheric signatures that is consistent with a high metallicity ($> 300\times$ Solar) cloudy atmosphere, consistent with subsequent eclipse observations

from JWST (Mukherjee et al. 2025). Similar high metallicity interpretations were inferred from CRIRES+ observations of the $2 R_\oplus$ sub-Neptune GJ3090b (Parker et al. 2025). JWST observations of other mature-aged sub-Neptunes have also found a predominance of such high metallicity atmospheres (e.g., TOI-836c, Wallack et al. 2024; GJ 9827 d, Piaulet-Ghorayeb et al. 2024; GJ 1214 b, Gao et al. 2023). Such heavy atmospheres may still be the end product of photoevaporation in gas-rich planets (e.g., Chen & Rogers 2016; Malsky & Rogers 2020), or they may be steam-based atmospheres in volatile-rich planets (e.g., Venturini et al. 2020; Bitsch et al. 2021).

Within this context, we demonstrated that we are close to the point where ground-based observations can help rule out high metallicity atmospheres in scenarios such as HIP94235b. If the planet has such a high metallicity atmosphere, it would be similar to other small planets surveyed so far. The lack of active escape signatures and the high metallicity is consistent with the interpretation that either small planets are the end product of runaway mass loss, or that they are born with heavy, volatile rich envelopes. Differentiating between these scenarios will require observations of younger sub-Neptunes, for which density and mass loss rates between the two models should be substantially different (e.g. Rogers 2025).

We respectfully acknowledge the traditional custodians of all lands throughout Australia, and recognise their continued cultural and spiritual connection to the land, waterways, cosmos, and community. We pay our deepest respects to all Elders, ancestors and descendants of the Giabal, Jarowair, and Kambuwal nations, upon whose lands this research was conducted. GZ and AM thank the support of the ARC DECRA program DE210101893 and ARC Future Fellowship award FT230100517. CH thanks the support of the ARC DECRA program DE200101840 and ARC Future Fellowship award FT240100016.

Facility: VLT, TESS

Software: emcee (Foreman-Mackey et al. 2013), batman (Kreidberg 2015), astropy (Astropy Collaboration et al. 2018), PyAstronomy (Czesla et al. 2019), pycirres (Stolker & Landman 2023)

REFERENCES

- Alam, M. K., Kirk, J., Dos Santos, L. A., et al. 2024, AJ, 168, 102
- Allart, R., Bourrier, V., Lovis, C., et al. 2018, Science, 362, 1384

- Astropy Collaboration, Price-Whelan, A. M., Sipőcz, B. M., et al. 2018, *AJ*, 156, 123
- Barat, S., Désert, J.-M., Goyal, J. M., et al. 2024a, *A&A*, 692, A198
- Barat, S., Désert, J.-M., Vazan, A., et al. 2024b, *Nature Astronomy*, 8, 899
- Basilicata, M., Giacobbe, P., Bonomo, A. S., et al. 2024, *A&A*, 686, A127
- Bitsch, B., Raymond, S. N., Buchhave, L. A., et al. 2021, *A&A*, 649, L5
- Broggi, M., Giacobbe, P., Guilluy, G., et al. 2018, *A&A*, 615, A16
- Chen, H., & Rogers, L. A. 2016, *ApJ*, 831, 180
- Clough, S. A., Iacono, M. J., & Moncet, J.-L. 1992, *J. Geophys. Res.*, 97, 15,761
- Czesla, S., Schröter, S., Schneider, C. P., et al. 2019, *PyA: Python astronomy-related packages*, ascl:1906.010
- Dorn, R. J., Bristow, P., Smoker, J. V., et al. 2023, *A&A*, 671, A24
- Dos Santos, L. A., Vidotto, A. A., Vissapragada, S., et al. 2022, *A&A*, 659, A62
- Foreman-Mackey, D., Hogg, D. W., Lang, D., & Goodman, J. 2013, *PASP*, 125, 306
- Gaia Collaboration, Brown, A. G. A., Vallenari, A., et al. 2021, *A&A*, 649, A1
- Gaidos, E., Hirano, T., Mann, A. W., et al. 2020, *MNRAS*, 495, 650
- Gaidos, E., Hirano, T., Lee, R. A., et al. 2023, *MNRAS*, 518, 3777
- Gao, P., Piette, A. A. A., Steinrueck, M. E., et al. 2023, *ApJ*, 951, 96
- Gibson, N. P., Merritt, S., Nugroho, S. K., et al. 2020, *MNRAS*, 493, 2215
- Ginzburg, S., Schlichting, H. E., & Sari, R. 2016, *ApJ*, 825, 29
- Ginzburg, S., Schlichting, H. E., & Sari, R. 2018, *Monthly Notices of the Royal Astronomical Society*, 476, 759
- Grasser, N., Snellen, I. A. G., Landman, R., Picos, D. G., & Gandhi, S. 2024, *A&A*, 688, A191
- Guillot, T. 2010, *A&A*, 520, A27
- Guilluy, G., D'Arpa, M. C., Bonomo, A. S., et al. 2024, *A&A*, 686, A83
- Gullikson, K., Dodson-Robinson, S., & Kraus, A. 2014, *AJ*, 148, 53
- Hauschildt, P. H., Allard, F., & Baron, E. 1999, *ApJ*, 512, 377
- Henden, A. A., Templeton, M., Terrell, D., et al. 2016, *VizieR Online Data Catalog: AAVSO Photometric All Sky Survey (APASS) DR9 (Henden+, 2016)*, *VizieR On-line Data Catalog: II/336*. Originally published in: 2015AAS...22533616H
- Kreidberg, L. 2015, *PASP*, 127, 1161
- Lee, E. J., Chiang, E., & Ormel, C. W. 2014, *ApJ*, 797, 95
- Lopez, E. D., Fortney, J. J., & Miller, N. 2012, *ApJ*, 761, 59
- Malsky, I., & Rogers, L. A. 2020, *ApJ*, 896, 48
- Mandel, K., & Agol, E. 2002, *ApJL*, 580, L171
- Mansfield, M., Bean, J. L., Oklopčić, A., et al. 2018, *ApJL*, 868, L34
- Mollière, P., van Boekel, R., Bouwman, J., et al. 2017, *A&A*, 600, A10
- Mollière, P., Wardenier, J. P., van Boekel, R., et al. 2019, *A&A*, 627, A67
- Morrissey, A., Zhou, G., Huang, C. X., et al. 2024, *AJ*, 168, 141
- Mukherjee, S., Schlawin, E., Bell, T. J., et al. 2025, *arXiv e-prints*, arXiv:2502.17418
- Ninan, J. P., Stefansson, G., Mahadevan, S., et al. 2020, *ApJ*, 894, 97
- Oklopčić, A. 2019, *ApJ*, 881, 133
- Oklopčić, A., & Hirata, C. M. 2018, *ApJL*, 855, L11
- Orell-Miquel, J., Murgas, F., Pallé, E., et al. 2024, *A&A*, 689, A179
- Owen, J. E., & Wu, Y. 2017, *The Astrophysical Journal*, 847, 29
- Palle, E., Nortmann, L., Casasayas-Barris, N., et al. 2020, *A&A*, 638, A61
- Parker, L. T., Mendonça, J. M., Diamond-Lowe, H., et al. 2025, *arXiv e-prints*, arXiv:2503.16608
- Piaulet-Ghorayeb, C., Benneke, B., Radica, M., et al. 2024, *arXiv e-prints*, arXiv:2410.03527
- Ribas, I., Guinan, E. F., Güdel, M., & Audard, M. 2005, *ApJ*, 622, 680
- Rogers, J. G. 2025, *arXiv e-prints*, arXiv:2503.17364
- Rogers, J. G., Dorn, C., Aditya Raj, V., Schlichting, H. E., & Young, E. D. 2025, *ApJ*, 979, 79
- Rogers, J. G., & Owen, J. E. 2021, *MNRAS*, 503, 1526
- Seager, S., & Sasselov, D. D. 2000, *ApJ*, 537, 916
- Skrutskie, M. F., Cutri, R. M., Stiening, R., et al. 2006, *AJ*, 131, 1163
- Spake, J. J., Sing, D. K., Evans, T. M., et al. 2018, *Nature*, 557, 68
- Stolker, T., & Landman, R. 2023, *pycrites: Data reduction pipeline for VLT/CRIRES+*, *Astrophysics Source Code Library*, record ascl:2307.040
- Tamuz, O., Mazeh, T., & Zucker, S. 2005, *MNRAS*, 356, 1466

- Thao, P. C., Mann, A. W., Feinstein, A. D., et al. 2024, *AJ*, 168, 297
- Turner, J. D., Christie, D., Arras, P., Johnson, R. E., & Schmidt, C. 2016, *MNRAS*, 458, 3880
- Venturini, J., Guilera, O. M., Haldemann, J., Ronco, M. P., & Mordasini, C. 2020, *A&A*, 643, L1
- Vidal-Madjar, A., & des Etangs, A. L. 2003, "Osiris" (HD209458b), an evaporating planet, [arXiv:astro-ph/0312382](https://arxiv.org/abs/astro-ph/0312382)
- Wallack, N. L., Batalha, N. E., Alderson, L., et al. 2024, *AJ*, 168, 77
- Zeng, L., Jacobsen, S. B., Sasselov, D. D., et al. 2019, *Proceedings of the National Academy of Science*, 116, 9723
- Zhang, M., Knutson, H. A., Dai, F., et al. 2023, *AJ*, 165, 62
- Zhang, M., Knutson, H. A., Wang, L., et al. 2022, *AJ*, 163, 68
- Zhou, G., Wirth, C. P., Huang, C. X., et al. 2022, *The Astronomical Journal*, 163, 289